

A quantum dot in germanium proximitized by a superconductor

Lazar Lakić^{†,1}, William Iain L. Lawrie^{†,1}, David van Driel,² Lucas E. A. Stehouwer,² Yao Su,¹ Menno Veldhorst,² Giordano Scappucci,² Ferdinand Kuemmeth,¹ and Anasua Chatterjee^{1,2,*}

¹*Center for Quantum Devices, Niels Bohr Institute,
University of Copenhagen, 2100 Copenhagen, Denmark*

²*QuTech and Kavli Institute of Nanoscience, Delft University of Technology, Delft, The Netherlands*
(Dated: December 3, 2024)

Planar germanium quantum wells have recently been shown to host hard-gapped superconductivity. Additionally, quantum dot spin qubits in germanium are well-suited for quantum information processing, with isotopic purification to a nuclear spin-free material expected to yield long coherence times. Therefore, as one of the few group IV materials with the potential to host superconductor-semiconductor hybrid devices, proximitized quantum dots in germanium is a compelling platform to achieve and combine topological superconductivity with existing and novel qubit modalities. Here we demonstrate a quantum dot (QD) in a Ge/SiGe heterostructure proximitized by a platinum germanosilicide (PtGeSi) superconducting lead (SC), forming a SC-QD-SC junction. We show tunability of the QD-SC coupling strength, as well as gate control of the ratio of charging energy and the induced gap. We further exploit this tunability by exhibiting control of the ground state of the system between even and odd parity. Furthermore, we characterize the critical magnetic field strengths, finding a critical out-of-plane field of 0.90 ± 0.04 T. Finally we explore sub-gap spin splitting in the device, observing rich physics in the resulting spectra, that we model using a zero-bandwidth model in the Yu-Shiba-Rusinov limit. The demonstration of controllable proximitization at the nanoscale of a germanium quantum dot opens up the physics of novel spin and superconducting qubits, and Josephson junction arrays in a group IV material.

INTRODUCTION

New and exotic physical phenomena can emerge in superconducting-semiconducting hybrids, enabling engineered quantum materials [1], circuit quantum electrodynamics (cQED) with novel superconducting qubits [2, 3], and topologically protected phases [4–7]. In particular, proximitized quantum dots constitute key building blocks for devices such as Cooper pair splitters [8], Kitaev chains [6, 7], and protected qubits [9, 10]. However, to date the majority of these experiments have been performed in group III-V materials where nuclear spins are unavoidable, critically hampering spin coherence, and where 2D heterostructures exhibit piezoelectricity, deleterious for cQED circuits [11]. Conversely, silicon and germanium are established group IV material platforms to integrate spin qubits hosted in gate defined quantum dots [12, 13], with isotopic purification having proved crucial for ultra-long spin qubit coherence [14]. Contrary to silicon [15], germanium forms low resistance Ohmic contacts due to intrinsic Fermi level pinning close to the valence band [16, 17]. This has motivated a strong effort to induce superconductivity [18–23] and very recently, signs of hard-gap superconductivity have been observed in mesoscopic devices implemented in a Ge/SiGe heterostructure [22, 23], in Ge/Si core shell nanowires [24–26] and in a cQED circuit [27].

Here, we present a superconducting-semiconducting hybrid quantum dot, which is hosted in Ge, a group IV material uniquely allowing for both isotopic purification [28] and a superconducting hard gap [22, 23]. Our demonstration in a two-dimensional heterostruc-

ture establishes a novel platform that exhibits enhanced scalability compared to nanowires, is compatible with radiofrequency-reflectometry readout [29] and a highly successful spin qubit platform [30–32]. It may therefore be useful for extending the range of qubit interactions, by using crossed Andreev reflection [33, 34] as well as heterogeneous quantum processors [9, 35] incorporating spin [12, 13] and superconducting circuits [36]. Isotopically purified, proximitized germanium may enable coherent Andreev spin qubits, protected superconducting qubits, and quantum dot-based Kitaev chains, and our demonstration of a quantum dot with gate-tunable proximitization in a group IV heterostructure is a key ingredient.

In this work, superconducting polycrystalline Platinum-Germanium-silicide (PtSiGe) leads are formed by a controlled thermally-activated solid phase reaction between deposited platinum (Pt) and the heterostructure (Ge/SiGe) [22]. Importantly, the PtGeSi leads alleviate the need to etch into the heterostructure to deposit or pattern the superconductor, a potential source of damage exposing the quantum well and interface to oxygen and processing. This method of achieving a transparent interface to a superconductor, via a reaction with a deposited noble metal, constitutes a general technique that has been exploited in other materials [38–40]. The leads act as charge reservoirs and as a source of proximitization for the quantum dot (QD). We first demonstrate Coulomb blockade physics of a QD coupled to two superconducting leads (SC) forming a SC-QD-SC junction. We identify a superconducting gap energy window of $4\Delta_0 = 284 \mu\text{eV}$ inside which transport is suppressed, and outside which standard

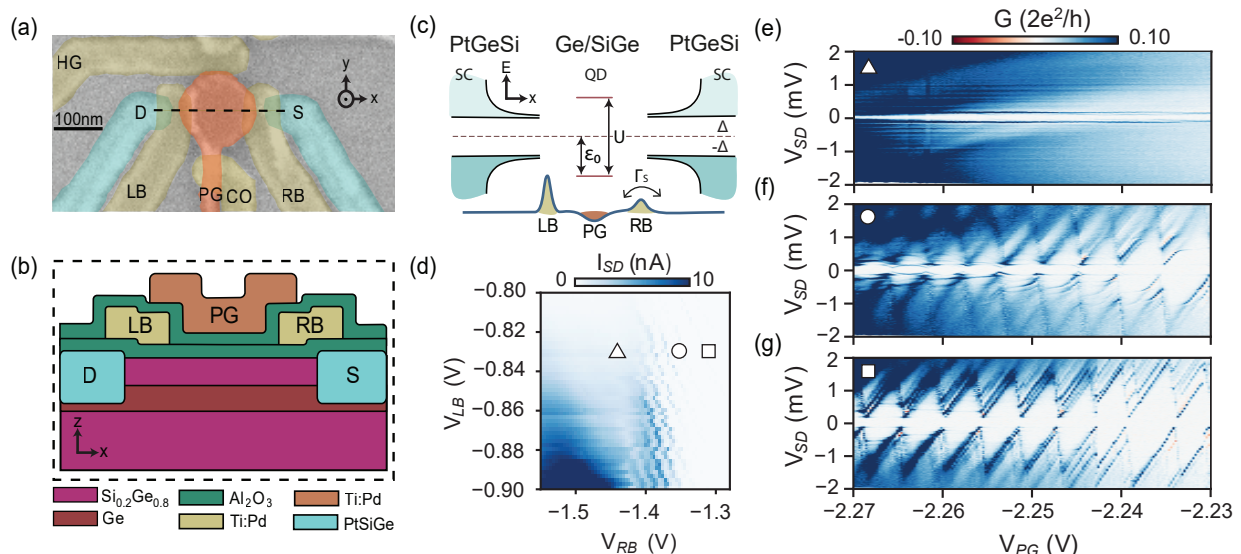


FIG. 1. (a) False coloured scanning electron micrograph (SEM) of a nominally identical device. The device comprises three lithographically defined metallic layers, separated by a dielectric of Al_2O_3 grown using atomic layer deposition (ALD). A plunger gate PG (orange) controls the electrochemical potential of the quantum dot. The coupling of the quantum dot to the superconducting PtSiGe leads S and D is controlled by two barrier gates LB and RB (yellow). A cut-off gate CO prevents accumulation beneath the gate fan-out of PG, and a helper gate HG provides further control of the quantum dot confinement. (b) Heterostructure and gate stack schematic corresponding to the cross section indicated by the black dashed line in (a). (c) Energy schematic depicting the physical system in (a). Here, Δ is the SC gap energy, U the charging energy of the QD, Γ_S the hybridization energy of the SC and QD and ϵ_0 the electrochemical potential of the QD with respect to the SC Fermi energy. (d) Source-drain current I_{SD} as a function of barrier gates V_{LB} and V_{RB} at bias voltage $V_{SD} = 300 \mu\text{V}$, $V_{PG} = -2.22 \text{ V}$, and $V_{HG} = -1.00 \text{ V}$. The square, circle and triangle correspond to the indicated gate voltage setting in (e), (f) and (g). Horizontal features likely correspond to charge instabilities in the environment surrounding the quantum dot. (e-g) Bias spectroscopy for the three gate voltages indicated in (d), with high, moderate and low coupling of the quantum dot to the superconducting leads respectively, showing a transition between strongly coupled lead (e) and weakly coupled lead (g). Negative differential conductance observed may indicate Coulomb diamonds of odd occupancy [37].

Coulomb diamonds are recovered. The charging energy of the system is typically larger than 1 meV, making it the dominating energy scale. Consequentially, Yu-Shiba-Rusinov (YSR) physics is expected to describe the observed phenomena. We observe sub-gap states in transport upon increasing the QD-SC coupling Γ_S , which is consistent with the formation of YSR states in the system [41, 42]. We demonstrate gate control of Γ_S by tuning the ground state at half-filling from a singlet state to a doublet state [43]. We then study the critical magnetic field of the hybrid device, finding an out-of-plane critical magnetic field $B_{\perp}^c = 0.90 \pm 0.04 \text{ T}$. Finally, we investigate spin-splitting in the SC-QD-SC system, finding a g -factor of 1.5 ± 0.2 for an out-of-plane magnetic field, and also characterize the g -tensor anisotropy. To explain the energy splitting observed in the SC-QD-SC system we use a zero bandwidth (ZBW) Anderson Impurity model [44, 45] with the possibility of Zeeman splitting on the SC. Our observation of controllable subgap states and subgap spin splitting, magnetic field resilience, and the high tunability of the quantum dot-superconducting coupling establishes Ge/SiGe and PtSiGe as an attractive platform for hybrid quantum

information processing.

RESULTS

We utilize established fabrication protocols for QD fabrication [46] and superconducting contacts [22] in Ge/SiGe quantum wells [47], to create a quantum dot coupled to two superconducting leads formed by rapid thermal annealing of Pt at 400°C in Ar atmosphere for 15 minutes. Figure 1a shows a false-colored scanning electron micrograph of the device, consisting of one lithographically-defined layer for the superconducting leads (cyan) and two layers of electrostatic gates (yellow and orange, see Methods and section I for further details). Figure 1b shows a schematic of the cross-section of the device heterostructure and gate stack. Layers are electrically isolated from one another by 7 nm of Al_2O_3 deposited by atomic layer deposition at 150°C . Barrier gates (LB, RB) control Γ_S , while the plunger gate (PG) controls the relative electrochemical potential of the quantum dot levels with respect to the superconducting leads (ϵ_0) as seen in Figure 1c. Two gates (HG and

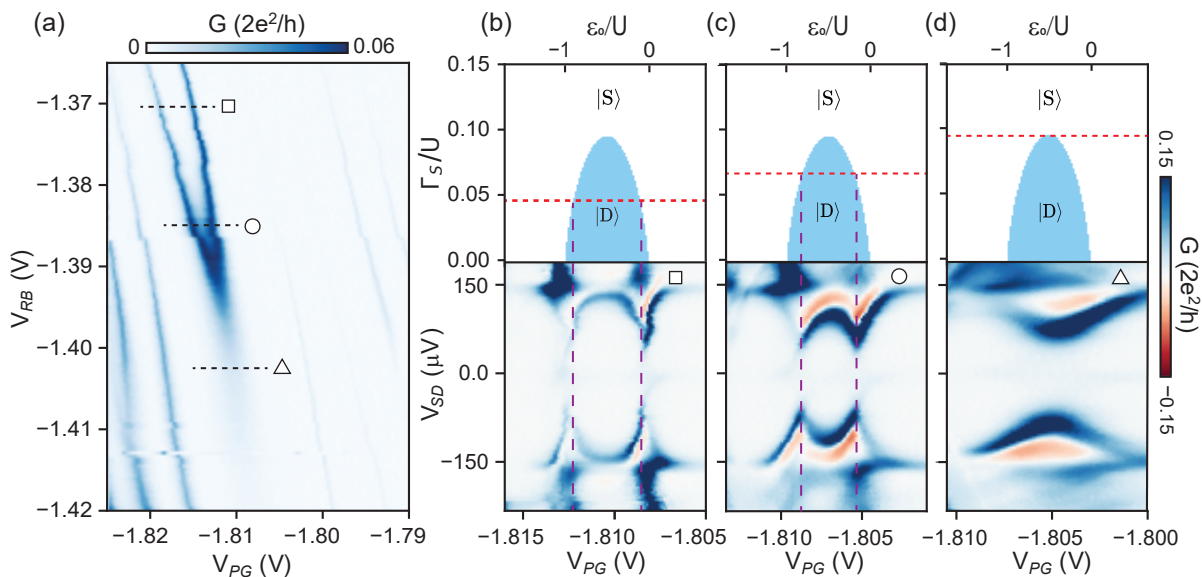


FIG. 2. **(a)** Charge stability diagram of V_{RB} vs V_{PG} at $V_{SD} = 80 \mu\text{V}$, $V_{LB} = -1.108 \text{ V}$, and $V_{HG} = -1.000 \text{ V}$. A cross-capacitance between the electrostatic gate V_{RB} and the quantum dot results in simultaneous tuning of Γ_S and ϵ_0 . We note that we expect the quantum dot system to be in the multi-hole regime. **(b-d)** Bottom panels show bias spectroscopy at decreasing values of V_{RB} corresponding to the square, circle, and triangle icons in panel a. Upper panels portray phase diagrams for the singlet and doublet phases, computed using a minimal ZBW model of the expected ground state character of the hybrid system. Here, ϵ_0 is the electrochemical potential of the quantum dot with respect to the grounded superconducting leads, and U is the charging energy of the quantum dot, the phase diagram was computed assuming $U = 1.6 \text{ meV}$ and $\Delta = 71 \mu\text{eV}$. As the SC-QD coupling Γ_S is increased, the doublet state becomes energetically unfavorable, as seen by the merging of charge transitions (magenta dashed lines). Γ_S is roughly estimated by modelling the sub-gap spectrum in the bottom panels (see Supplementary Information section V), to be $70 \mu\text{eV}$, $110 \mu\text{eV}$, and $150 \mu\text{eV}$ from b-d respectively, as indicated by the red dashed lines.

CO) are also used to confine (HG) the quantum dot and prevent unwanted accumulation (CO). We utilize standard DC transport and low frequency lock-in techniques to measure source-drain current I_{SD} and differential conductance G across the quantum dot. Notably, our device is also connected to a radiofrequency (RF) reflectometry circuit via the source superconducting lead, both techniques described in Supplementary Information section I. Additional datasets in the low-coupling regime measured using this RF probe are presented in the Supplementary Information section II.

All data are taken at a lock-in frequency of 119 Hz, and amplitude of $2.5 \mu\text{V}$. Figure 1d shows I_{SD} as a function of the tunnel barrier V_{LB} and V_{RB} . Here, the source drain bias energy is set to $eV_{SD} = 300 \mu\text{eV}$ such that it exceeds the expected zero-field superconducting gap energy of $\sim 70 \mu\text{eV}$ [22]. We set V_{LB} close to its pinch-off value such that it acts as a tunnel probe, and vary V_{RB} to tune the coupling between superconductor and quantum dot Γ_S (Figure 1c). This limits current through the device to around 1 nA, which we estimate to be well within the critical current density of the superconducting leads (See Supplementary Figure S6b). Figures 1e-g show bias spectroscopy at different values of V_{RB} . In the strong coupling regime (Figure 1e), we

observe a range in bias energy of $4\Delta_0$ where transport is suppressed, from which we extract a superconducting pairing amplitude of $\Delta_0 = 71 \pm 6 \mu\text{eV}$, in its fully open state. The apparent reduction of the SC gap upon increased V_{PG} is attributed to sub-gap transport phenomena due to increased junction transparency [48]. We furthermore note that the dark features outside of the SC gap likely result from out of gap structure in the SC leads [49]. Figure 1f shows that as Γ_S is decreased (positive change on V_{RB}), we observe tunnel-broadened Coulomb oscillations and sub-gap transport features, indicating a hybridized QD. At low coupling between the QD and SC (Fig. 1g) we observe sharp Coulomb diamonds outside a bias window of $\pm 2\Delta_0$. We conclude that we have versatile electrostatic control of the degree of hybridization of a quantum dot with a superconductor, consistent with experiments performed in InAs-Al nanowires [50] and InSbAs-Al 2DEGs [6].

Singlet-doublet quantum phase transition

A quantum dot coupled to a superconducting lead at half-occupancy of charges can have two different ground states, depending on the degree of superconductor-quantum dot coupling. At low coupling strengths and

zero magnetic field strength, the ground state at half-filling, ie. $\epsilon_0/U = 0.5$, will be a spin-degenerate doublet state $|D\rangle = \{|\downarrow\rangle, |\uparrow\rangle\}$. Here, ϵ_0 is the electrochemical potential of the QD with respect to the SC lead and U is the charging energy of the QD. At high coupling, a preference for superconducting pairing will dominate, leading to a singlet ground state $|S\rangle = u|0\rangle - v|2\rangle$. We stress that the labeling of these states is not representative of the localization of the charges between superconductor and quantum dot, and rather a convenient pedagogical representation of the basis states of the system. As a result of U being the dominant energy scale, the system is firmly in the YSR limit. By utilizing the control of Γ_S demonstrated above, we show that we can tune between these ground states. We operate in a regime whereby V_{LB} is very close to its pinch-off value, such that it acts as a tunneling probe. We then vary V_{RB} to tune the coupling Γ_S . Figure 2a shows a charge stability diagram of the system with the QD plunger gate V_{PG} on the horizontal axis, and the QD-SC barrier gate V_{RB} on the vertical axis, at a bias energy of $eV_{SD} = 80 \mu\text{eV}$, slightly above Δ . The vertical lines measured are Coulomb resonances indicating transitions between the N , $N+1$ and $N+2$ occupations of the quantum dot (from right to left). As we increase Γ_S by making RB more negative we observe the merging of two levels at approximately $V_{RB} = -1.395 \text{ V}$.

We further investigate these transitions with bias spectroscopy as a function of plunger gate voltage at different values of V_{RB} . In the bottom panel of Figure 2b, we show bias spectroscopy at $V_{RB} = -1.3717 \text{ V}$ (square in Figure 2a) for varying V_{SD} and V_{PG} . At V_{PG} values of -1.812 V and -1.808 V , the state crosses Δ_0 , signalling the changes in ground state parity as seen from 2a.

In the bottom panel of Figure 2c, we show spectroscopy at $V_{RB} = -1.3850 \text{ V}$ (circle in Figure 2a). We see an evolution of the state features into a characteristic eye-shape indicating the formation of YSR states [41, 51–54] on the hybridized QD. The negative differential conductance is attributed to probing sub-gap features with a coherence peak [55]. In the bottom panel of Figure 2d, we perform bias spectroscopy at $V_{RB} = -1.4025 \text{ V}$ (triangle in Figure 2a) showing no parity change, which we interpret as the QD filling remaining in a singlet ground state upon loading an additional hole.

In QD-SC systems, where the charging energy of the QD U is larger than the SC order parameter Δ , quasiparticles in the SC can bind to the dot by the exchange interaction and give rise to sub-gap excitations in the form of YSR states. Such systems can be modelled using a zero-bandwidth (ZBW) model that describes a quantum dot coupled to a single superconducting orbital [44, 56], which predicts which ground state the system prefers depending on the degree of hybridization between the SC and the QD. By solving the ZBW model for where the energy of the singlet equals the one of the doublet, a singlet doublet phase transition diagram can be realized. In the

top panels of Figure 2b-d such a phase transition has been computed using a ZBW model with a charging energy of $U = 1.6 \text{ meV}$ and a superconducting gap of $\Delta = 71 \mu\text{eV}$, the dashed lines have been inserted at Γ_S values based on extracted coupling values ($70 \mu\text{eV}$, $110 \mu\text{eV}$, and $150 \mu\text{eV}$ from b-d respectively) divided by U , also using the aforementioned minimal ZBW model (see Supplementary Information section V). As the hybridization energy Γ_S increases, it becomes less favorable to maintain the $|D\rangle$ ground state. The horizontal dashed lines thus indicate a qualitative correspondence between the experimental barrier gate RB controlling Γ_S , and the calculated Γ_S in the phase diagram. The magenta stippled lines in the bottom panels serve as guides to the eye to indicate where the phase transitions occur.

Magnetic field characterization

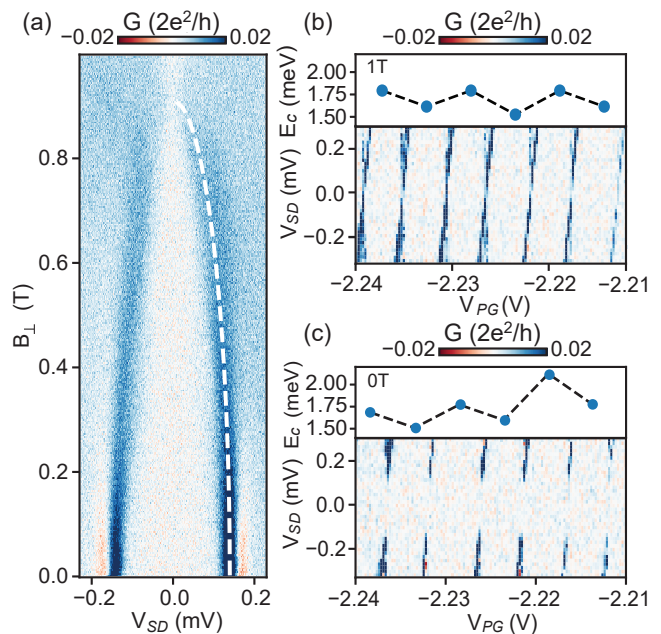


FIG. 3. (a) Bias spectroscopy as a function of out-of-plane magnetic field B_{\perp} , with $V_{PG} = -2.225 \text{ V}$, $V_{HG} = 1.000 \text{ V}$, $V_{RB} = -1.450 \text{ V}$ and $V_{LB} = -0.825 \text{ V}$. We extract a critical field $B_{c,\perp} = 0.90 \pm 0.04 \text{ T}$. (b-c) Bias spectroscopy at low Γ_S $V_{RB} = -1.300 \text{ V}$, $V_{LB} = -0.825 \text{ V}$, and $V_{HG} = -1.000 \text{ V}$ for out-of-plane magnetic field $B_{\perp} = 1 \text{ T}$, and $B_{\perp} = 0 \text{ T}$ respectively. Top panels show extracted charging energies from Coulomb diamonds below.

We now turn to the magnetic field dependence of the superconducting parent gap. Figure 3a shows bias spectroscopy of the quantum dot in the few hole and low Γ_S regime, as a function of out-of-plane magnetic field strength B_{\perp} . We fit the closing of the superconducting gap according to $\Delta(B) = 2\Delta_0\sqrt{1 - (B/B_c)^2}$ [57], where Δ_0 is the superconducting gap at zero magnetic

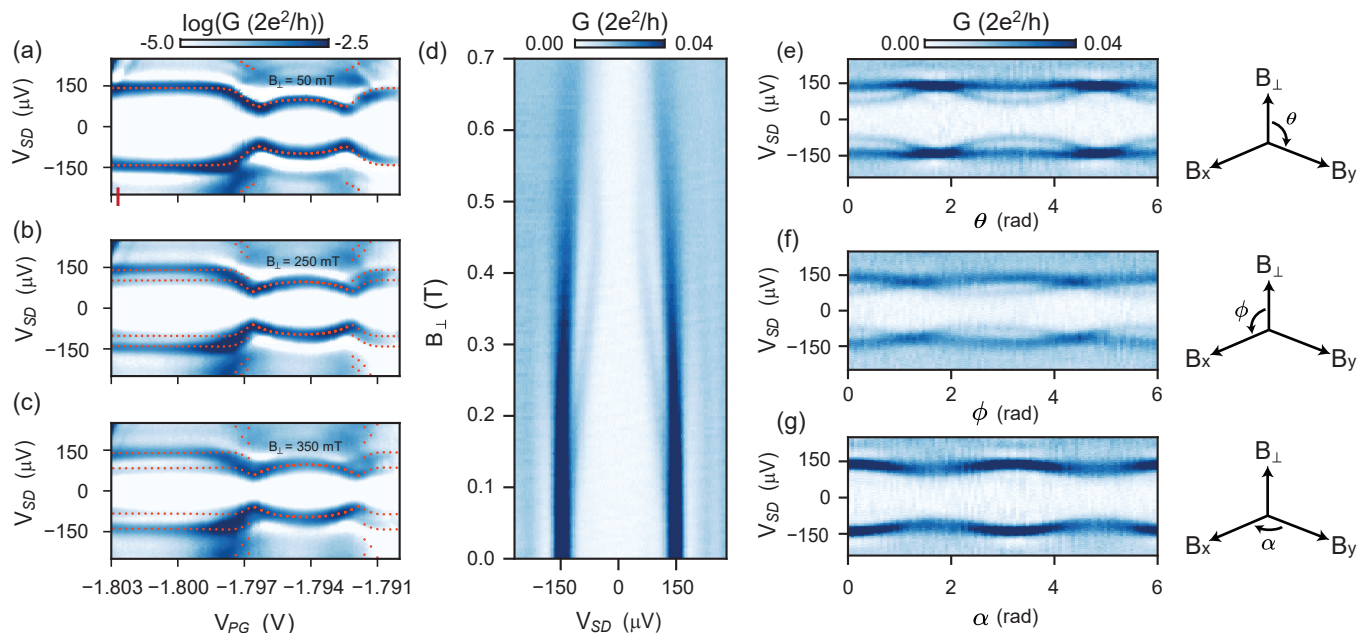


FIG. 4. **(a-c)** Bias spectroscopy displayed in logarithmic scale at magnetic field strengths of 50 mT, 250 mT and 350 mT respectively, with the barrier gates set to $V_{RB} = -1.4100$ V, $V_{LB} = -0.8070$ V and $V_{HG} = -0.9575$ V. Sub-gap energy splitting is visible in b) and c). The superimposed orange markers in Figures a-c serve as a qualitative comparison between the measured transport data and calculations using a zero-bandwidth model, inputting a $\Delta = 71$ μeV , hybridization energy $\Gamma_S = 110$ μeV , charging energy $U = 1.6$ meV, as well as a Zeeman energy of $E_z^{SC} = 4$ μeV on the SC and $E_z^{QD} = 4$ μeV on the QD, $E_z^{SC} = 44$ μeV on the SC and $E_z^{QD} = 44$ μeV on the QD, and $E_z^{SC} = 56$ μeV on the SC and $E_z^{QD} = 56$ μeV on the QD, respectively. **(d)** Magnetic field sweep at $V_{RB} = -1.4100$ V, $V_{LB} = -0.8070$ V, $V_{HG} = -0.9575$ V, and $V_{PG} = -1.8027$ V tuned within the singlet ground state, as indicated by the red notch in a). We extract a g -factor for the out-of-plane magnetic field splitting $g_{\perp} = 1.5 \pm 0.2$. **(e-g)** Bias spectroscopy of rotating magnetic field at total magnetic field strength $|B| = 420$ mT and $V_{PG} = -1.8028$ V, also tuned to the singlet groundstate. Strong g -tensor anisotropy is observed between out-of-plane and in-plane magnetic field orientations.

field, and B_c is the critical magnetic field. We extract a critical field of $B_{c,\perp} = 0.90 \pm 0.04$ T. This greatly exceeds the critical field measured in prior studies, where the critical out-of-plane magnetic field was measured to be approximately 50 mT [22]. This disparity could be due to the smaller size of the superconducting junctions and leads [58] measured in the present experiment compared to those in ref. [22], which may alleviate vortex formation (see Supplementary section IV.). We also characterize the critical magnetic field strengths for the two in-plane axes in Supplementary Section III. Figures 3b and 3c show bias spectroscopy of the quantum dot in the low coupling limit, taken at 1 T and 0 T respectively. At 0 T the superconducting gap is present within the Coulomb diamonds (Figure 3b), while normal Coulomb diamonds are recovered at 1 T due to the breaking down of superconductivity (Figure 3c). In both cases we find an even-odd oscillation in the filling structure at both low and high field strengths as seen in the top panels of Figures 3b and 3c, depicting the addition energy of each Coulomb diamond below, consistent with that observed previously in germanium [59] and InAs [51] QDs. The charging energy of the quantum dot varies between even

and odd periodicity, indicating that the quantum dot is in the low hole occupancy. The charging energy is typically between 1 and 1.8 meV, more than ten times the superconducting gap, supporting our interpretation that we are in the YSR regime.

Finally we study the transport spectrum under the influence of a magnetic field in the same electrostatic regime as Figure 2b-c. Figures 4a-c show bias spectroscopy measurements as a function of V_{PG} portrayed in logarithmic scale for enhanced visibility, taken at a perpendicular magnetic field, at strengths of (a) 50 mT, (b) 250 mT, and (c) 350 mT (see Supplementary Figures S7a-b for data in non-logarithmic scale). At 50 mT a $|S\rangle\text{-}|D\rangle\text{-}|S\rangle$ transition spectrum is observed, as seen in Figure 2b-c. A qualitative ZBW model of the system is plotted on top of the data as described previously (see Supplementary section V for details of the model), using a SC pairing energy of $\Delta_0 = 71$ μeV , a hybridization energy of $\Gamma_S = 110$ μeV , and a QD charging energy of $U = 1.6$ meV. As we increase the perpendicular field an energy splitting of the subgap states is observed in the singlet ground-state sectors 4b-c. Interestingly, the en-

ergy splitting seen in the even parity groundstates have a flat energy dispersion indicating either a spin splitting of the parent gap itself, or of a strongly coupled sub-gap state, which we attribute to spinful excited quasiparticles. To qualitatively model the data, we introduce a Zeeman splitting term into the ZBW model for both the SC and QD. We find that setting the g -factor of the QD and superconducting orbitals to be equal in magnitude is sufficient to phenomenologically model the data potentially due to a g -factor renormalization as a result of hybridization [60, 61]. Additional data at lower magnetic field strength and lower coupling, supporting our hypothesis of g -factor renormalization, is reported in the Supplementary section II, as well as results from our ZBW model with varying system parameters in Supplementary section V.

In Figure 4d, we set the plunger gate voltage to $V_{\text{PG}} = -1.8027$ such that the quantum dot is in a singlet ground state as indicated by the red notch in Figure 4a and perform bias spectroscopy as a function of B_{\perp} from 0 T to 0.7 T. We observe the magnetic field splitting of the superconducting coherence peaks, and extract an out-of-plane g -factor, $g_{\perp} = 1.5 \pm 0.2$. This value is several times larger than the g -factor measured for magnetic fields close to in-plane in planar germanium quantum wells [62, 63], and several times smaller than the value reported in ref. [64] for out of plane g -factors. Furthermore, in a regime of lower coupling for the YSR states, we have measured an out-of-plane g -factor of $g_{\perp} = 4.5 \pm 0.6$ (see Supplementary Information, Figure S1) and a $g_{\perp} = 5.3 \pm 0.8$ in out-of-gap Coulomb diamond spectroscopy (see Supplementary Information, Figure S2). These observations support the hypothesis that the g -factor g_{\perp} either describes the quasiparticle coherence peaks, or is due to renormalization of the Ge/SiGe hole g -factor as a result of hybridization with the superconductor [60, 61].

Finally, we investigate anisotropy of the g -factor by performing bias spectroscopy as a function of magnetic field orientation. Figures 4e-g show bias spectroscopy at a magnetic field strength of $|B| = 420$ mT. The splitting is then investigated as a function of rotation angles. Here, the rotation angles θ , ϕ and α are defined as shown in Figure 4e-g. A large anisotropy is measured; while g -tensor anisotropy is ubiquitous for heavy holes in strained planar Ge/SiGe wells, it is seldom observed for a superconducting gap edge. On the other hand, anisotropic g -tensors have been observed in heavy fermion bulk superconductors, which could additionally explain the non-dispersive splitting in Fig. 4b-c [65]. We stress that our use of the annealed poly-crystalline superconductor Pt-GeSi is a recent material development in itself, and the physics of superconductivity in these nanoscale thin films is not fully understood. However, this anisotropy could also be explained by a sub-gap state in the QD that is

strongly coupled to the superconductor.

CONCLUSION

We have demonstrated a quantum dot in Ge/SiGe proximitized by a superconducting lead and exhibiting clear YSR states. We find that the coupling between quantum dot and superconducting lead is highly tunable, as evidenced by the tunnel barrier controllability of the singlet or doublet nature of the YSR ground state at half-filling. Additionally, we have characterized the critical magnetic field strength, finding an out-of-plane critical field of ~ 0.90 T. Finally, we observe Zeeman splitting of sub-gap states, which we explain using a modified zero-bandwidth Anderson impurity model. The ability to tune and strongly couple a superconductor to a quantum dot, in combination with a critical magnetic field, demonstrates the feasibility of our platform for hybrid germanium quantum information processing, including Andreev spin qubits and topological quantum computing, as well as the exploration of fundamental physics with superconductor-semiconductor devices. While the in-plane g -tensor component of holes in germanium planar wells is lower than in established group III-V platforms, it could be enhanced by confinement-induced g -factor engineering [66], and the out-of-plane g -factor could provide an alternative route to engineering topologically protected qubits using QD-SC chains [67]. Further work on RF-reflectometry-based measurements (as described in the Supplementary Information section I and II) could help achieve charge sensing and parity readout. Additionally, studying the dependence of the parent gap and induced gap as a function of temperature and coupling strength would elucidate the nature of the superconducting proximitization of PtSiGe on Ge/SiGe quantum dots [48]. Finally, our work motivates the exploration of alternative materials beyond platinum that also form superconducting germanide phases, such as iridium, rhodium [68], and niobium [69], with the goal of identifying a germanosilicide capable of hosting large superconducting gap energies while being compatible with the fabrication process of Ge/SiGe heterostructures [46]. Our demonstration in a group IV material, amenable to isotopic purification, constitutes a crucial building block for superconducting-semiconducting hybrid technologies and opens up previously inaccessible experimental directions.

[†] These authors contributed equally.

AUTHOR INFORMATION

L.E.A.S and G.S. grew and supplied the Ge/SiGe heterostructures and developed processes for the PtGeSi

contacts. L.L. and W.I.L.L. designed the devices. L.L. fabricated the devices. L.L. and W.I.L.L. performed the experiment in the dilution refrigerator along with D.v.D. and Y.S., and analysed the data. L.L. performed numerical simulations within the ZBW model with help from D.v.D. and W.I.L.L. L.L. and W.I.L.L. wrote the manuscript with input from D.v.D., M.V., G.S., F.K. and A.C. A.C. and F.K. supervised the project.

ACKNOWLEDGMENTS

We thank J. Paaske, V. Baran and G. Mazur for valuable discussions. This project has received funding from the European Research Council (ERC) as part of the project NONLOCAL under grant agreement No 856526, and through the IGNITE project under grant agreement No. 101069515 of the Horizon Europe Framework Programme. AC acknowledges support from the Inge Lehmann Programme of the Independent Research Fund Denmark. We acknowledge funding by the Casimir PhD Travel Grant.

DATA AVAILABILITY

Raw data and analysis scripts for all data included in this work are available at the Zenodo data repository at <https://doi.org/10.5281/zenodo.14237057>.

* anasua.chatterjee@tudelft.nl

- [1] C. G. L. Böttcher, F. Nichele, M. Kjaergaard, H. J. Suominen, J. Shabani, C. J. Palmstrøm, and C. M. Marcus, Superconducting, insulating and anomalous metallic regimes in a gated two-dimensional semiconductor–superconductor array, *Nature Physics* **14**, 1138 (2018).
- [2] M. Hays, V. Fatemi, D. Bouman, J. Cerrillo, S. Diamond, K. Serniak, T. Connolly, P. Krogstrup, J. Nygård, A. L. Yeyati, A. Geresdi, and M. H. Devoret, Coherent manipulation of an Andreev spin qubit, *Science* **373**, 430 (2021).
- [3] A. Bargerboos, M. Pita-Vidal, R. Zitko, L. J. Splitthoff, L. Grunhaupt, J. J. Wesdorp, Y. Liu, L. P. Kouwenhoven, R. Aguado, C. K. Andersen, A. Kou, and B. van Heck, Spectroscopy of spin-split Andreev levels in a quantum dot with superconducting leads, *Phys. Rev. Lett.* **131**, 097001 (2023).
- [4] M. Leijnse and K. Flensberg, Parity qubits and poor man’s Majorana bound states in double quantum dots, *Phys. Rev. B* **86**, 134528 (2012).
- [5] A. Y. Kitaev, Unpaired Majorana fermions in quantum wires, *Physics-Uspekhi* **44**, 131 (2001).
- [6] S. L. ten Haaf, Q. Wang, A. M. Bozkurt, C.-X. Liu, I. Kulesh, P. Kim, D. Xiao, C. Thomas, M. J. Manfra, T. Dvir, *et al.*, Engineering Majorana bound states in coupled quantum dots in a two-dimensional electron gas, arXiv preprint [arXiv:2311.03208](https://arxiv.org/abs/2311.03208) (2023).
- [7] T. Dvir, G. Wang, N. van Loo, C.-X. Liu, G. P. Mazur, A. Bordin, S. L. Ten Haaf, J.-Y. Wang, D. van Driel, F. Zatelli, *et al.*, Realization of a minimal Kitaev chain in coupled quantum dots, *Nature* **614**, 445 (2023).
- [8] G. Wang, T. Dvir, G. P. Mazur, C.-X. Liu, N. van Loo, S. L. D. ten Haaf, A. Bordin, S. Gazibegovic, G. Badawy, E. P. A. M. Bakkers, M. Wimmer, and L. P. Kouwenhoven, Singlet and triplet Cooper pair splitting in hybrid superconducting nanowires, *Nature* **612**, 448 (2022).
- [9] D. M. Pino, R. S. Souto, and R. Aguado, Minimal Kitaev-transmon qubit based on double quantum dots, *Phys. Rev. B* **109**, 075101 (2024).
- [10] Q. Wang, S. L. D. ten Haaf, I. Kulesh, D. Xiao, C. Thomas, M. J. Manfra, and S. Goswami, Triplet correlations in Cooper pair splitters realized in a two-dimensional electron gas, *Nature Communications* **14**, 4876 (2023).
- [11] M. Scigliuzzo, L. E. Bruhat, A. Bengtsson, J. J. Burnett, A. F. Roudsari, and P. Delsing, Phononic loss in superconducting resonators on piezoelectric substrates, *New Journal of Physics* **22**, 053027 (2020).
- [12] G. Burkard, T. D. Ladd, A. Pan, J. M. Nichol, and J. R. Petta, Semiconductor spin qubits, *Rev. Mod. Phys.* **95**, 025003 (2023).
- [13] G. Scappucci, C. Kloeffel, F. A. Zwanenburg, D. Loss, M. Myronov, J.-J. Zhang, S. De Franceschi, G. Katsaros, and M. Veldhorst, The germanium quantum information route, *Nature Reviews Materials* **6**, 926 (2021).
- [14] J. T. Muhonen, J. P. Dehollain, A. Laucht, F. E. Hudson, R. Kalra, T. Sekiguchi, K. M. Itoh, D. N. Jamieson, J. C. Mccallum, A. S. Dzurak, and A. Morello, Storing quantum information for 30 seconds in a nanoelectronic device, *Nature Nanotechnology* **9**, 986 (2014).
- [15] M. Tao, S. Agarwal, D. Udeshi, N. Basit, E. Maldonado, and W. P. Kirk, Low Schottky barriers on n-type silicon (001), *Applied Physics Letters* **83**, 2593 (2003).
- [16] A. Dimoulas, P. Tsipas, A. Sotiropoulos, and E. K. Evangelou, Fermi-level pinning and charge neutrality level in germanium, *Applied Physics Letters* **89**, 252110 (2006).
- [17] T. Nishimura, K. Kita, and A. Toriumi, Evidence for strong Fermi-level pinning due to metal-induced gap states at metal/germanium interface, *Applied Physics Letters* **91**, 123123 (2007).
- [18] K. Aggarwal, A. Hofmann, D. Jirovec, I. Prieto, A. Sammak, M. Botifoll, S. Marti-Sanchez, M. Veldhorst, J. Arbiol, G. Scappucci, J. Danon, and G. Katsaros, Enhancement of proximity-induced superconductivity in a planar ge hole gas, *Phys. Rev. Res.* **3**, L022005 (2021).
- [19] F. Vigneau, R. Mizokuchi, D. C. Zanuz, X. Huang, S. Tan, R. Maurand, S. Frolov, A. Sammak, G. Scappucci, F. Lefloch, and S. De Franceschi, Germanium quantum-well Josephson field-effect transistors and interferometers, *Nano Letters* **19**, 1023 (2019).
- [20] N. W. Hendrickx, D. P. Franke, A. Sammak, M. Kouwenhoven, D. Sabbagh, L. Yeoh, R. Li, M. L. V. Tagliaferri, M. Virgilio, G. Capellini, G. Scappucci, and M. Veldhorst, Gate-controlled quantum dots and superconductivity in planar germanium, *Nature Communications* **9**, 2835 (2018).
- [21] J. Ridderbos, M. Brauns, J. Shen, F. K. de Vries, A. Li, E. P. A. M. Bakkers, A. Brinkman, and F. A. Zwanenburg, Josephson effect in a few-hole quantum dot, *Advanced Materials* **30**, 1802257 (2018).

- [22] A. Tosato, V. Levajac, J.-Y. Wang, C. J. Boor, F. Borsoi, M. Botifoll, C. N. Borja, S. Marti-Sanchez, J. Arbiol, A. Sammak, M. Veldhorst, and G. Scappucci, Hard superconducting gap in germanium, *Communications Materials* **4**, 23 (2023).
- [23] M. Valentini, O. Sagi, L. Baghumyan, T. de Gijzel, J. Jung, S. Calcaterra, A. Ballabio, J. Aguilera Servin, K. Aggarwal, M. Janik, T. Adletzberger, R. Seoane Souto, M. Leijnse, J. Danon, C. Schrade, E. Bakkers, D. Chrastina, G. Isella, and G. Katsaros, Parity-conserving Cooper-pair transport and ideal superconducting diode in planar germanium, *Nature Communications* **15**, 169 (2024).
- [24] J. Ridderbos, M. Brauns, F. K. de Vries, J. Shen, A. Li, S. Kölling, M. A. Verheijen, A. Brinkman, W. G. van der Wiel, E. P. A. M. Bakkers, and F. A. Zwanenburg, Hard superconducting gap and diffusion-induced superconductors in Ge-Si nanowires, *Nano Lett.* **20**, 122 (2020).
- [25] E. Zhuo, Z. Lyu, X. Sun, A. Li, B. Li, Z. Ji, J. Fan, E. P. A. M. Bakkers, X. Han, X. Song, F. Qu, G. Liu, J. Shen, and L. Lu, Hole-type superconducting gatemon qubit based on Ge/Si core/shell nanowires, *npj Quantum Information* **9**, 51 (2023).
- [26] H. Zheng, L. Y. Cheung, N. Sangwan, A. Kononov, R. Haller, J. Ridderbos, C. Ciaccia, J. H. Ungerer, A. Li, E. P. A. M. Bakkers, A. Baumgartner, and C. Schönenberger, Coherent control of a few-channel hole type gatemon qubit, *Nano Lett.* **24**, 7173 (2024).
- [27] M. Hinderling, S. ten Kate, M. Coraiola, D. Haxell, M. Stiefel, M. Mergenthaler, S. Paredes, S. Bedell, D. Sabonis, and F. Nichele, Direct microwave spectroscopy of Andreev bound states in planar Ge Josephson junctions, *arXiv preprint arXiv:2403.03800* (2024).
- [28] K. Itoh, W. Hansen, E. Haller, J. Farmer, V. Ozhogin, A. Rudnev, and A. Tikhomirov, High purity isotopically enriched ^{70}Ge and ^{74}Ge single crystals: Isotope separation, growth, and properties, *Journal of Materials Research* **8**, 1341–1347 (1993).
- [29] F. Vigneau, F. Fedele, A. Chatterjee, D. Reilly, F. Kuemmeth, M. F. Gonzalez-Zalba, E. Laird, and N. Ares, Probing quantum devices with radio-frequency reflectometry, *Applied Physics Reviews* **10**, 021305 (2023).
- [30] F. Borsoi, N. W. Hendrickx, V. John, M. Meyer, S. Motz, F. van Riggelen, A. Sammak, S. L. de Snoo, G. Scappucci, and M. Veldhorst, Shared control of a 16 semiconductor quantum dot crossbar array, *Nature Nanotechnology* **19**, 21 (2024).
- [31] N. W. Hendrickx, W. I. L. Lawrie, M. Russ, F. van Riggelen, S. L. de Snoo, R. N. Schouten, A. Sammak, G. Scappucci, and M. Veldhorst, A four-qubit germanium quantum processor, *Nature* **591**, 580 (2021).
- [32] D. Jirovec, A. Hofmann, A. Ballabio, P. M. Mutter, G. Tavani, M. Botifoll, A. Crippa, J. Kukucka, O. Sagi, F. Martins, *et al.*, A singlet-triplet hole spin qubit in planar Ge, *Nature Materials* **20**, 1106 (2021).
- [33] M. Leijnse and K. Flensberg, Coupling spin qubits via superconductors, *Phys. Rev. Lett.* **111**, 060501 (2013).
- [34] M. Spethmann, S. Bosco, A. Hofmann, J. Klinovaja, and D. Loss, High-fidelity two-qubit gates of hybrid superconducting-semiconducting singlet-triplet qubits, *Physical Review B* **109**, 085303 (2024).
- [35] A. Gyenis, A. Di Paolo, J. Koch, A. Blais, A. A. Houck, and D. I. Schuster, Moving beyond the transmon: Noise-protected superconducting quantum circuits, *PRX Quantum* **2**, 030101 (2021).
- [36] M. Kjaergaard, M. E. Schwartz, J. Braumüller, P. Krantz, J. I.-J. Wang, S. Gustavsson, and W. D. Oliver, Superconducting qubits: Current state of play, *Annual Review of Condensed Matter Physics* **11**, 369 (2020).
- [37] S. De Franceschi, L. Kouwenhoven, C. Schoenenberger, and W. Wernsdorfer, Hybrid superconductor–quantum dot devices, *Nature Nanotechnology* **5**, 703 (2010).
- [38] M. Bai, F. Yang, M. Luysberg, J. Feng, A. Bliesener, G. Lippertz, A. A. Taskin, J. Mayer, and Y. Ando, Novel self-epitaxy for inducing superconductivity in the topological insulator $(\text{Bi}_{1-x}\text{Sb}_x)_2\text{Te}_3$, *Phys. Rev. Mater.* **4**, 094801 (2020).
- [39] I. T. Rosen, C. J. Trimble, M. P. Andersen, E. Mikheev, Y. Li, Y. Liu, L. Tai, P. Zhang, K. L. Wang, Y. Cui, M. A. Kastner, J. R. Williams, and D. Goldhaber-Gordon, Fractional AC Josephson effect in a topological insulator proximitized by a self-formed superconductor, *Physical Review B* **110** (2024).
- [40] Y. Jia, G. Yu, T. Song, F. Yuan, A. J. Uzan, Y. Tang, P. Wang, R. Singha, M. Onyszczyk, Z. J. Zheng, K. Watanabe, T. Taniguchi, L. M. Schoop, and S. Wu, Superconductivity from on-chip metallization on 2d topological chalcogenides, *Phys. Rev. X* **14**, 021051 (2024).
- [41] G. Kirsanskas, M. Goldstein, K. Flensberg, L. I. Glazman, and J. Paaske, Yu-Shiba-Rusinov states in phase-biased superconductor–quantum dot–superconductor junctions, *Phys. Rev. B* **92**, 235422 (2015).
- [42] A. Jellinggaard, K. Grove-Rasmussen, M. H. Madsen, and J. Nygaard, Tuning yu-shiba-rusinov states in a quantum dot, *Phys. Rev. B* **94**, 064520 (2016).
- [43] A. Bargerbos, M. Pita-Vidal, R. Zitko, J. Avila, L. J. Splitthoff, L. Grunhaupt, J. J. Wesdorp, C. K. Andersen, Y. Liu, L. P. Kouwenhoven, R. Aguado, A. Kou, and B. van Heck, Singlet-doublet transitions of a quantum dot Josephson junction detected in a transmon circuit, *PRX Quantum* **3**, 030311 (2022).
- [44] J. Bauer, A. Oguri, and A. C. Hewson, Spectral properties of locally correlated electrons in a Bardeen–Cooper–Schrieffer superconductor, *Journal of Physics: Condensed Matter* **19**, 486211 (2007).
- [45] T. Meng, S. Florens, and P. Simon, Self-consistent description of Andreev bound states in Josephson quantum dot devices, *Physical Review B* **79**, 224521 (2009).
- [46] W. I. L. Lawrie, H. G. J. Eenink, N. W. Hendrickx, J. M. Boter, L. Petit, S. V. Amitonov, M. Lodari, B. Paquelet Wuetz, C. Volk, S. G. J. Philips, G. Droulers, N. Kalhor, F. van Riggelen, D. Brousse, A. Sammak, L. M. K. Vandersypen, G. Scappucci, and M. Veldhorst, Quantum dot arrays in silicon and germanium, *Applied Physics Letters* **116**, 080501 (2020).
- [47] A. Sammak, D. Sabbagh, N. W. Hendrickx, M. Lodari, B. Paquelet Wuetz, A. Tosato, L. Yeoh, M. Bollani, M. Virgilio, M. A. Schubert, P. Zaumseil, G. Capellini, M. Veldhorst, and G. Scappucci, Shallow and undoped germanium quantum wells: A playground for spin and hybrid quantum technology, *Advanced Functional Materials* **29**, 1807613 (2019).
- [48] M. Kjaergaard, H. J. Suominen, M. P. Nowak, A. R. Akhmerov, J. Shabani, C. J. Palmström, F. Nichele, and C. M. Marcus, Transparent semiconductor–superconductor interface and induced gap in an epitaxial heterostructure Josephson junction, *Phys. Rev. Appl.* **7**,

- 034029 (2017).
- [49] Z. Su, A. Zarassi, J.-F. Hsu, P. San-Jose, E. Prada, R. Aguado, E. J. H. Lee, S. Gazibegovic, R. L. M. O. het Veld, D. Car, S. R. Plissard, M. Hocevar, M. Pendharkar, J. S. Lee, J. A. Logan, C. J. Palmstrøm, E. P. A. M. Bakkers, and S. M. Frolov, Mirage Andreev spectra generated by mesoscopic leads in nanowire quantum dots, *Phys. Rev. Lett.* **121**, 127705 (2018).
- [50] E. J. H. Lee, X. Jiang, M. Houzet, R. Aguado, C. M. Lieber, and S. De Franceschi, Spin-resolved Andreev levels and parity crossings in hybrid superconductor–semiconductor nanostructures, *Nature Nanotechnology* **9**, 79 (2014).
- [51] K. Grove-Rasmussen, H. I. Jorgensen, B. M. Andersen, J. Paaske, T. S. Jespersen, J. Nygaard, K. Flensberg, and P. E. Lindelof, Superconductivity-enhanced bias spectroscopy in carbon nanotube quantum dots, *Phys. Rev. B* **79**, 134518 (2009).
- [52] L. Yu, Bound states in paramagnetic impurity-containing superconductors, *Chinese Journal of Physics* **21**, 21 (1965).
- [53] H. Shiba, Classical Spins in Superconductors, *Progress of Theoretical Physics* **40**, 435 (1968).
- [54] A. I. Rusinov, Superconductivity near a paramagnetic impurity, *Letters to JETP* **9**, 146 (1969).
- [55] B. M. Andersen, K. Flensberg, V. Koerting, and J. Paaske, Nonequilibrium transport through a spinful quantum dot with superconducting leads, *Phys. Rev. Lett.* **107**, 256802 (2011).
- [56] V. V. Baran, E. J. Frost, and J. Paaske, Surrogate model solver for impurity-induced superconducting sub-gap states, *Physical Review B* **108**, L220506 (2023).
- [57] M. Tinkham, *Introduction to Superconductivity*, 2nd ed. (Dover Publications, 2004).
- [58] P. Fulde, High field superconductivity in thin films, *Advances in Physics* **22**, 667 (1973).
- [59] F. van Riggelen, N. W. Hendrickx, W. I. L. Lawrie, M. Russ, A. Sammak, G. Scappucci, and M. Veldhorst, A two-dimensional array of single-hole quantum dots, *Applied Physics Letters* **118**, 044002 (2021).
- [60] M. W. A. de Moor, J. D. S. Bommer, D. Xu, G. W. Winkler, A. E. Antipov, A. Bargerbos, G. Wang, N. van Loo, R. L. M. O. het Veld, S. Gazibegovic, D. Car, J. A. Logan, M. Pendharkar, J. S. Lee, E. P. A. M. Bakkers, C. J. Palmstrøm, R. M. Lutchyn, L. P. Kouwenhoven, and H. Zhang, Electric field tunable superconductor–semiconductor coupling in Majorana nanowires, *New Journal of Physics* **20**, 103049 (2018).
- [61] A. E. Antipov, A. Bargerbos, G. W. Winkler, B. Bauer, E. Rossi, and R. M. Lutchyn, Effects of gate-induced electric fields on semiconductor Majorana nanowires, *Phys. Rev. X* **8**, 031041 (2018).
- [62] N. W. Hendrickx, D. P. Franke, A. Sammak, G. Scappucci, and M. Veldhorst, Fast two-qubit logic with holes in germanium, *Nature* **577**, 487 (2020).
- [63] N. W. Hendrickx, W. I. L. Lawrie, L. Petit, A. Sammak, G. Scappucci, and M. Veldhorst, A single-hole spin qubit, *Nature Communications* **11**, 3478 (2020).
- [64] N. W. Hendrickx, L. Massai, M. Mergenthaler, F. J. Schupp, S. Paredes, S. W. Bedell, G. Salis, and A. Fuhrer, Sweet-spot operation of a germanium hole spin qubit with highly anisotropic noise sensitivity, *Nature Materials* **23**, 920 (2024).
- [65] P. Chandra, P. Coleman, and R. Flint, Hysteric order in the heavy-fermion compound URu₂Si₂, *Nature* **493**, 621 (2013).
- [66] S. Bosco, M. Benito, C. Adelsberger, and D. Loss, Squeezed hole spin qubits in Ge quantum dots with ultrafast gates at low power, *Phys. Rev. B* **104**, 115425 (2021).
- [67] K. Laubscher, J. D. Sau, and S. Das Sarma, Germanium-based hybrid semiconductor–superconductor topological quantum computing platforms: Disorder effects, arXiv preprint [arXiv:2404.16285](https://arxiv.org/abs/2404.16285) (2024).
- [68] B. T. Matthias, T. H. Geballe, and V. B. Compton, Superconductivity, *Rev. Mod. Phys.* **35**, 1 (1963).
- [69] B. Langa, D. Sapkota, I. Lainez, R. Haight, B. Srijanto, L. Feldman, H. Hijazi, X. Zhu, L. Hu, M. Kim, and K. Sardashti, Solid-state reactions at niobium–germanium interfaces in hybrid superconductor–semiconductor devices, arXiv preprint [arXiv:2405.20517](https://arxiv.org/abs/2405.20517) (2023).

METHODS

Fabrication

The device is fabricated on a Ge/SiGe heterostructure, which is grown on n-type Si(001) substrate using a reduced pressure chemical vapor deposition reactor. The stack comprises of a reverse graded $\text{Si}_{0.2}\text{Ge}_{0.8}$ virtual substrate, a 16 nm Ge quantum well, a 27 nm $\text{Si}_{0.2}\text{Ge}_{0.8}$ barrier, and a less than 1 nm Si sacrificial cap [47]. The device is fabricated in three electron-beam lithography defined layers separated by two oxide layers of ~ 7 nm Al_2O_3 grown with a Savannah Ultratech atomic layer deposition system at 150°C , using unheated Trimethyl Aluminium (TMA) precursor and unheated H_2O thermal co-reactant. The first layer forms the PtGeSi contacts defined by electron beam lithography using Kayaku 495 PMMA A2 polymer resist and AR 600-55 1:3 MIBK:IPA developer. Development is directly followed by a 60 s 100°C post bake on a hotplate before a wet etch is performed using buffered HF ($\sim 6\%$) solution to remove the sacrificial cap before a 15 nm Pt layer is deposited via e-gun evaporation at a pressure of 1×10^{-7} mbar. Lift-off is done in N-Methyl-2-Pyrrolidone (NMP), followed by 1,2-Dioxolane, and propan-2-ol (IPA) cleaning. The Pt contacts then undergo rapid thermal annealing at 400°C for 15 min in an argon atmosphere. Barrier gates and plunger gates are defined by electron beam lithography using AR-P 6200.04 polymer resist and N-amyl acetate developer, followed by an oxygen plasma ash. The barrier and plunger gates are deposited using electron-gun evaporation and consist of a Ti (5 nm) sticking layer and a Pd layer (25 nm and 29 nm for the barrier and plunger layers respectively). Lift-off is done in 1,2-Dioxolane, followed by 1,2-Dioxolane, propan-2-ol (IPA) and oxygen plasma ash cleaning.

Measurement

The device is measured inside a sample puck loaded into a Bluefors XLD dilution refrigerator, at a mixing chamber temperature of ~ 9 mK. The dilution refrigerator is equipped with a (1-1-6) T vector magnet, the sample chip being placed such that the 6 T direction is in-plane. We expect the main source of magnetic field misalignment to result from misalignment of the sample board inside the puck (QDevil QBoard sample holder) during sample loading. We estimate this error to be less than 5° . Differential conductance measurements are taken using a Stanford-Research Systems SR860 lock-in amplifier at a frequency of 119 Hz, and amplitude of $2.5 \mu\text{V}$ for all figures, except Figure 2a ($V_{AC} = 10 \mu\text{V}$), and Figure 4 ($V_{AC} = 3.2 \mu\text{V}$). A line resistance of $\sim 5.8 \text{ k}\Omega$ is subtracted in all measurements. Bias spectroscopy measurements contain a small thermally induced bias offsets on the order of $20 \mu\text{eV}$, which have been calibrated for and subtracted from all relevant datasets. DC gate voltages are applied via a QDevil QDAC-II voltage source. Additional information on the DC setup and components used can be found in Supplementary Information section I. In addition to lock-in measurements, radiofrequency reflectometry was performed as described in the Supplementary Information section I, using a FPGA with a built in microwave signal generator as well as signal demodulator (Quantum Machines OPX+). A tank circuit with a resonance frequency of 192.3 MHz was used, connected to the drain contact. The incident rf-signal is attenuated by 40 dB at various plates of the cryostat, and undergoes an additional attenuation of 20 dB from a directional coupler at the MXC plate (See Supplementary Section Figure I). The reflected signal undergoes 40 dB of amplification at the 4 K stage via a HEMT amplifier, and passes through a DC block and bias-tee at the input of the demodulation circuit. A 50Ω terminator is connected to the DC side of the bias-tee.

Supplementary Information: A quantum dot in germanium proximitized by a superconductor

Lazar Lakić^{†,1} William Iain L. Lawrie^{†,1} David van Driel,² Lucas E. A. Stehouwer,² Yao Su,¹
Menno Veldhorst,² Giordano Scappucci,² Ferdinand Kuemmeth,¹ and Anasua Chatterjee^{1,2,*}

¹*Center for Quantum Devices, Niels Bohr Institute,
University of Copenhagen, 2100 Copenhagen, Denmark*

²*QuTech and Kavli Institute of Nanoscience, Delft University of Technology, Delft, The Netherlands*
(Dated: December 3, 2024)

In the Supplementary Information we present additional data as well as a minimal model for our hybrid system. In section I, we present details on the experimental setup, describing both DC and RF measurements. In section II, we present data in a low regime of coupling between the superconductor (SC) and quantum dot (QD) that showcases the tunability of our system and complements the results presented in the main article. We also present similar results measured using radiofrequency (RF) reflectometry, a technique ubiquitous for spin-based qubits, crucial to develop readout for hybrid superconductor-semiconductor devices incorporating quantum dots, such as Kitaev chains. Section III describes critical field measurements for different orientations of the applied magnetic field. In Section IV we present data on PtSiGe Hall bars and wires providing an insight into the SC properties of PtSiGe films. Finally, Section V presents a qualitative model of the observed spectrum of our proximitized quantum dot.

Section I. Details of Experimental Setup

In this section we describe the experimental setup used for both the low-frequency (lock-in) measurements in the main text, and the RF-reflectometry setup used for the additional data presented in the supplement (Section II).

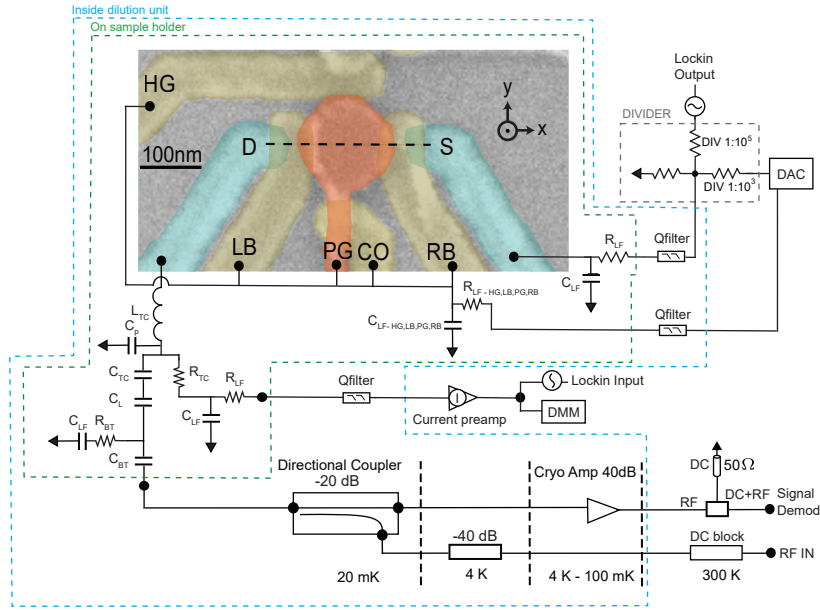


FIG. S1. False coloured SEM of a nominally identical device, including the experimental setup used for DC, differential conductance and RF measurements.

All measurements in Figures 1-4 in the main text are performed using a two-terminal measurement setup, measuring a DC current and/or the differential conductance G . For two-terminal measurements in which a DC current is measured, we apply a voltage on the source (S) via a QDevil DAC with a 16-bit resolution, and a ± 10 V output voltage. This voltage passes through a 1:1000 voltage divider on the DAC output. The voltage is applied to a DC-loom via a QFilter-II RC low pass filter ($f_{co}=65$ kHz) and LC low-pass filter ($f_{co}=225$ MHz), followed by a QDevil sampleboard incorporating further RC low-pass filtering ($f_{co} = 130$ kHz, $R_{LF} = 1.2$ k Ω , $C_{LF} = 1$ nF). The wirebond

connected to the drain contact connects to the PCB and branches into an RF-reflectometry setup, which is described below, and a DC readout line. The DC readout line on the drain (D) then passes through the same filtering setup as described above. Outside the cryostat, the voltage is converted to a current via a Basel SP983c current pre-amplifier set to a gain of 1×10^{-7} V/A before being digitized by a Keysight 34461A digital multimeter. The total line resistance of the sample board, QFilter-II, and DC looms amount to a line resistance of $R_{line} \sim 5.80 \pm 0.03$ k Ω .

The differential conductance measurements are performed by applying an AC excitation via a Stanford Research Systems SR860 lock-in amplifier. This excitation is combined with the DC signal via a 1:10000 voltage divider which otherwise undergoes the same filtering and amplification as the DC current. We furthermore subtract the line resistance of ~ 5.8 k Ω from each point on the V_{SD} axis, $V_{SD} = V_{DAC} - (I_{DC} \cdot R_{line})$, where V_{DAC} is the voltage being output from the DAC, I_{DC} is the measured current, and R_{line} the line resistance. We optimize and measure the in-phase component and convert the signal to units of quantum of conductance by $G = G_0^{-1} \cdot (\frac{V_{AC}}{X \cdot \text{Gain}} - R_{Line})^{-1}$, with $V_{AC} = 2.5$ μ V for all figures, except Figure 2a ($V_{AC} = 10$ μ V), and Figure 4 ($V_{AC} = 3.2$ μ V), X being the measured in-phase signal in units of volts, the Gain being 1×10^{-7} V/A, and $G_0 = 7.748091719 \times 10^{-5}$ S.

Furthermore, we incorporate high-frequency measurement via standard RF-reflectometry methods [1] using a cryogenic tank circuit with a frequency of 192.3 MHz (as seen in the measurements in the following section, in Figure S3). A typical RF excitation voltage at the sample is 3 μ V, which is applied and demodulated using a Quantum Machines OPX+. The RF-reflectometry setup has a bias-tee with resistance $R_{BT} = 50$ k Ω , capacitance $C_{BT} = 22$ nF, and an inductance $L_{TC} = 560$ nH. C_P is a parasitic capacitance that together with L_{TC} forms the resonant (tank) circuit, estimated to have a value of about 1.2 pF. The capacitances $C_{TC} = 100$ pF and $C_L = 100$ pF are coupling capacitances.

Section II. Low Γ_S B-field Studies in Transport and RF-Reflectometry

We study the magnetic field dependence of the subgap states in a regime of low coupling between SC and QD, complementary to the strong-coupling regime in the main text.

Setting the tunnel barriers to $V_{RB} = -1.39$ V and $V_{LB} = -0.8350$ V, we tune the QD into a many-hole regime using the plunger gate PG. We perform bias spectroscopy at 0 mT, observing filling of the QD with eye-like features characteristic of YSR states as described in the main text, and shown in Figure S2a. In Figure S2b the out-of-plane magnetic field is set to 100 mT, revealing lifting of what we believe is subgap spin degeneracy of the $|D\rangle$ groundstate, as indicated by the black arrows.

In Figure S2c the splitting is increased as shown by the black arrows, when we apply a field of 200 mT. We then configure the PG to $V_{PG} = -2.2365$ V at the subgap splitting in Figure S2c (orange notch), and vary the out-of-plane magnetic field as seen in Figure S2d. A Zeeman splitting is measured in bias spectroscopy starting from 0 mT. Extracting the g-factor using the standard the Zeeman formula yields a $g_{\perp} = 4.5 \pm 0.6$, consistent with previous experimental findings of large g-factors in planar Ge/SiGe, and ~ 3 times larger than the g-factor we found for the strongly hybridized system described in the main text in this study. As the magnetic field is rotated along the principal axis at a perpendicular field of 200 mT a strong anisotropy is seen, in agreement with previous studies carried out in planar Ge/SiGe.

We proceed to tune the QD to a few-hole regime and perform bias spectroscopy using standard RF-reflectometry methods as described above. Note that the Figures in S3 show the normalized demodulated signal V_{RF} .

Figures S3c-e depict Coulomb diamonds measured at magnetic field strengths of 0 mT, 750 mT and 990 mT respectively, in the few-hole, lower-coupling regime described in this Supplementary Information section. Suppression of transport exists in an energy window of gap of $\pm 2\Delta_0$, as well as Coulomb diamonds with charging energies exceeding 2 mV. The x-axis is labeled with a virtual parameter δV_{PG} , where $\delta V_{PG} = 0$ corresponds to $V_{PG} = -2$ V sweeping 15 mV above and below. Figures S3c-e depict bias spectroscopy from which we extract g_{\perp} outside the superconducting gap. Figures S3f-h correspond to zoomed-in plots of figures S3c-e, revealing a magnetic field dependent splitting. The extracted g-factor is $g = 5.3 \pm 0.8$, in agreement within error with the subgap spin splitting that we measured using low-frequency transport techniques, in Figure S2.

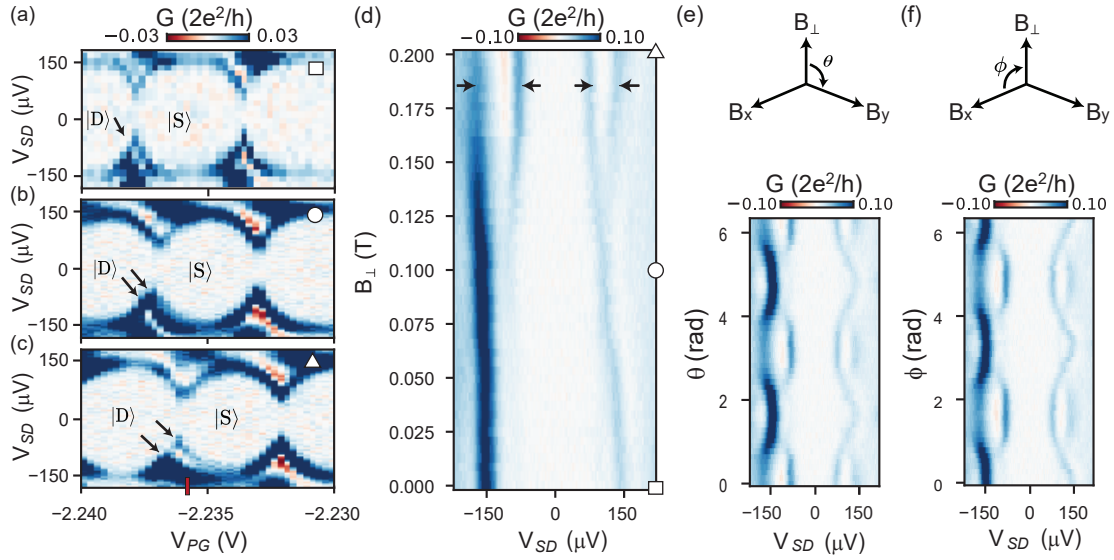


FIG. S2. **(a-c)** Bias spectroscopy with tunnel barriers set to $V_{RB} = -1.39$ V, $V_{LB} = -0.8350$ V, and $V_{HG} = -1$ V at 0 mT (square in (a)), 100 mT (circle in (b)) and 200 mT (triangle in (c)). Black arrows indicate spin splitting at the transition between a $|D\rangle$ groundstate and a $|S\rangle$ groundstate. **(d)** Magnetic field sweep at $V_{PG} = -2.2365$ V (red notch in (c)), showing spin-splitting of the odd-occupied state. We extract an out of plane g -factor of $g_{\perp} = 4.5 \pm 0.6$. **(e-f)** Bias spectroscopy as a function of magnetic field angle at total magnetic field strength $|B| = 200$ mT and $V_{PG} = -2.2365$ V. Above each panel, we state the rotational angle with respect to the sample direction. A strong g -tensor asymmetry is observed for the QD between out-of-plane and in-plane magnetic field orientations.

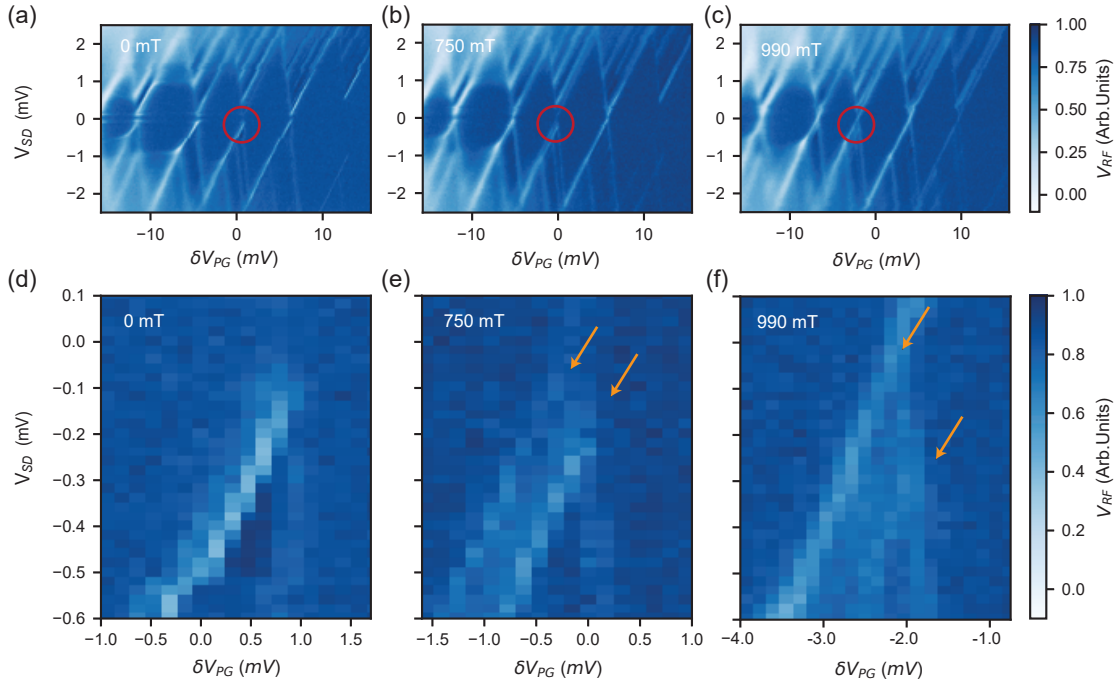


FIG. S3. **(a-c)** Bias spectroscopy, measured using RF reflectometry, at 0 mT (a) with electrostatic gates set to $V_{RB} = -1.48$, $V_{LB} = -1.11$ V, and $V_{HG} = 0$ V, 750 mT (b) and 990 mT (c). **(d-f)** Zoomed-in scan within the region marked by red circles in panels c-e respectively. Orange arrows indicate spin splitting, with a g -factor of $g = 5.3 \pm 0.8$.

Section III. Measurements of Critical Field

We perform bias spectroscopy as a function of magnetic field in Figure S4a-c, with the device configured in the few-hole regime. Figure S4b shows the critical in-plane field parallel to the direction of transport (see Figure S1a for a definition of the x direction). This configuration is expected to have a higher critical field than the perpendicular magnetic direction due to a smaller surface area, thus making it harder for the magnetic field flux to pin and destroy superconductivity. Finally, Figure S4c depicts the critical in-plane field perpendicular to the direction of transport (see Figure S1a for a definition of the y direction). The critical field in this direction is marginally lower than the out-of-plane magnetic field.

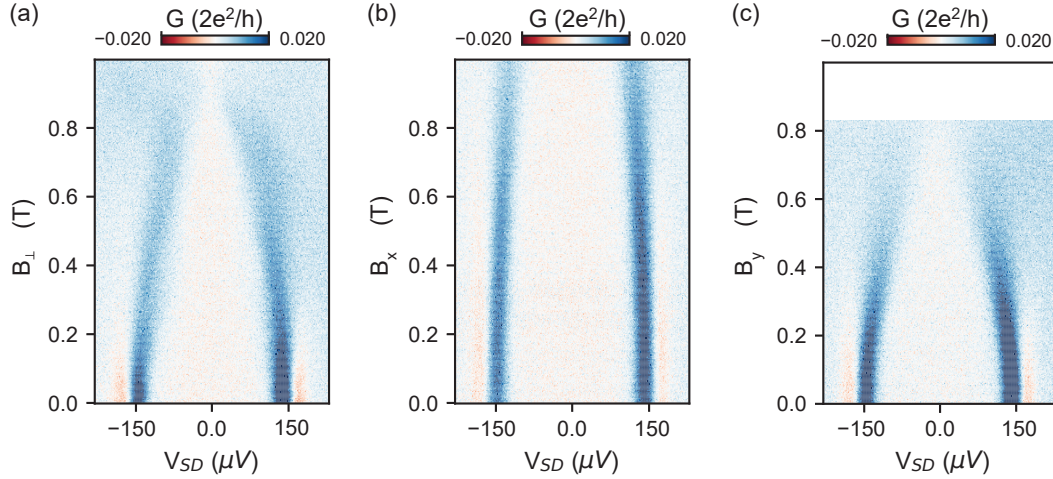


FIG. S4. Magnetic fields sweeps at same electrostatic gate settings as in main Figure 3a. **(a)** Magnetic field sweep from 0 to 1 T out of plane with respect to the device. **(b)** Magnetic field sweep from 0 to 1 T for in-plane field, parallel to the direction of transport **(c)** Magnetic field sweep from 0 to 0.82 T for in-plane field, perpendicular to the direction of transport.

	Device Type	B_x^* (T)	B_y^* (T)	B_\perp^* (T)
HB1	Hallbar	1.54(1)	-	-
HB2	Hallbar	>1	1.34(1)	0.474(1)
HB3	Hallbar	>1	>1	0.123(6)
SL1	Wire	0.831(6)	> 1	0.643(1)
SL2	Wire	0.827(1)	0.633(1)	0.695(1)*

TABLE I. Summary of measured critical magnetic fields for different Hall bar and wire devices under test. *We note that for wire SL2, two critical magnetic fields emerge, which we attribute to different geometries of the wire and the fanout. The number reported is the higher of the two critical fields. For completeness, the lower critical field occurs at $B_\perp = 0.500 \pm 0.001$ T.

Section IV. Electrical Characterization of PtSiGe Films

To study superconducting properties, we also perform measurements of the critical magnetic field strengths, for PtSiGe Hall bars and wires fabricated using identical methods and on the same wafer as the device reported in the manuscript. Figure S5a shows a schematic of the Hall bar dimensions and magnetic field orientation. We perform current bias measurements using a lock-in amplifier at 33 Hz excitation frequency and 0.5 V amplitude, applied through a 1 M Ω resistor. Figures S5b-d show measurements of differential resistance as a function of applied magnetic field strength for two separate Hall bars HB1 and HB2. Differential resistance is calculated by dividing the in-phase lock-in signals of the longitudinal voltage drop V_{xx} by the measured current at the drain electrode I . We fit a sigmoid function to the data of the form $R(B) = R_N/(1 + f(B))$ where $f(B) = \exp[-(B - B_c)/c]$. Here, R_N is the normal state resistance, B^c is the critical magnetic field, and c represents the broadening of the Normal-Superconducting transition. Critical magnetic fields for each Hall bar are reported in Table 1. As expected, the out-of-plane critical field B_\perp^c is smaller compared to the in-plane fields for a Hall Bar geometry, as observed in ref [2].

We also perform measurements of Critical magnetic fields on wires, whose geometries are shown in figure S5e. Two identical devices S1 and S2 are studied. Critical magnetic fields are reported in Table 1. We note that in figure S5h, there appear to be two transitions as shown using light and dark green. This is likely due to the design of the device, where the voltage probes will detect drops across part of the fanout, which have a much larger surface area than the wires themselves, resulting in a much smaller critical field. This is further evidenced when comparing the critical fields of the Hall bar devices and the wires, whereby the wires typically exhibit much higher out-of-plane critical magnetic fields.

We further study the electrical properties of the PtGeSi material, by measuring longitudinal and Hall resistances as a function of out of plane magnetic field, in Hall bar HB3 (Figure S6a). Sweeping magnetic field strength from -6 T to 6 T, we observe a linear dependence of the Hall resistance R_{xy} in the normal phase of the material. Fitting this, we extract a sheet carrier density of $n_{2D} = 5.2 \times 10^{16}$ cm $^{-2}$. We use this value combined with the longitudinal (normal) resistance $R_N = 37.9$ Ω , to extract a carrier mobility of $\mu = 6$ cm 2 /Vs.

Figure S6b shows current bias measurements through a wire device SL1, from which we extract a critical current of 4 μ A. Assuming a cross section of 100 nm x 15 nm for the wire, we calculate a critical current density of $J = 2.7$ A/m 2 . Due to the similarity in feature size, we expect this current density to reflect that of the superconducting leads in the device reported in the main manuscript. We note that measurements in the main text are taken at currents restricted to around 1 nA or lower (Main text Figure 1d) significantly lower than the expected critical current of 2.4 μ A, and are therefore unlikely to exhibit features due to depairing [3].

Finally, we study the critical temperature of the PtSiGe material in a wire device (SL2). We use a PID feedback loop on a heater placed at the Mixing chamber temperature stage of the cryostat, to control the temperature of the Mixing chamber plate. This temperature is stable within a range of ± 10 mK of the setpoint. We note that the temperature of the mixing chamber plate is not necessarily reflective of the temperature of the sample, as the sample is loaded inside a puck via a fast sample exchange unit, and is likely to underestimate the actual temperature by some tens of mK. We perform out-of-plane magnetic field sweeps between -0.2 T and 0.2 T, while stepping the mixing chamber temperature setpoint of the heater in steps of 20 mK, from 20 mK to 600 mK. After each temperature step, a settle time of 5 minutes is allowed before beginning the magnetic field sweep. Figure 6c shows the results of this measurement, indicating a clear switching between superconducting and normal phases. We fit the critical magnetic fields and critical temperatures using a sigmoid function, finding $T_c = 408$ mK, and $B_\perp^c = 0.116$ T. We plot the scaled phase diagram in figure S6d, and fit the standard BCS relation $T/T_c = 1.74\sqrt{1 - B_\perp/B_\perp^c}$ with good agreement.

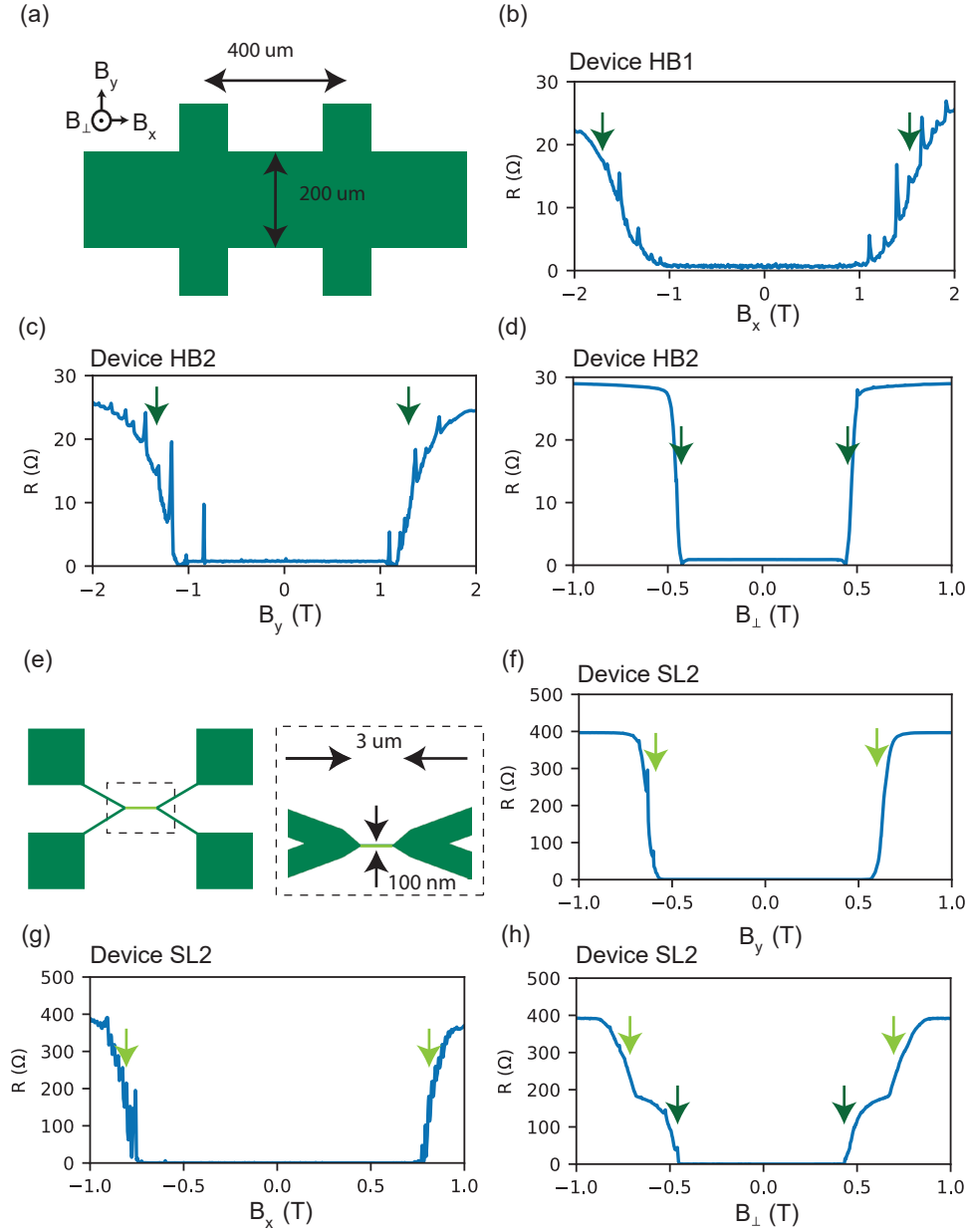


FIG. S5. **(a-d)** Critical magnetic field measurements for PtSiGe Hall bars. (a) Schematic of Hall bar geometry and alignment of magnetic field directions. Here, B_x indicates a magnetic field applied in the plane of the heterostructure, aligned with the direction of transport, B_y indicates a magnetic field applied in the plane of the heterostructure, perpendicular with the direction of transport, and B_{\perp} indicates a magnetic field applied out-of-plane with respect to the heterostructure. Dark green arrows represent the magnetic field at which a superconducting-normal state transition occurs according to the fit. **(e-g)** Critical magnetic field measurements for PtSiGe wires. (e) Schematic of wire geometry. The wires are $3 \mu\text{m}$ long, 100 nm wide, with a Pt deposition thickness of 15 nm . In (h), two critical magnetic field onsets occur due to the voltage probes being sensitive to voltage drops in part of the fanout (inset of (e)). The dark green arrows represent the superconducting-normal state transition of the larger ‘fanout’ section, while the light green arrows represent the superconducting-normal state transition of the wires.

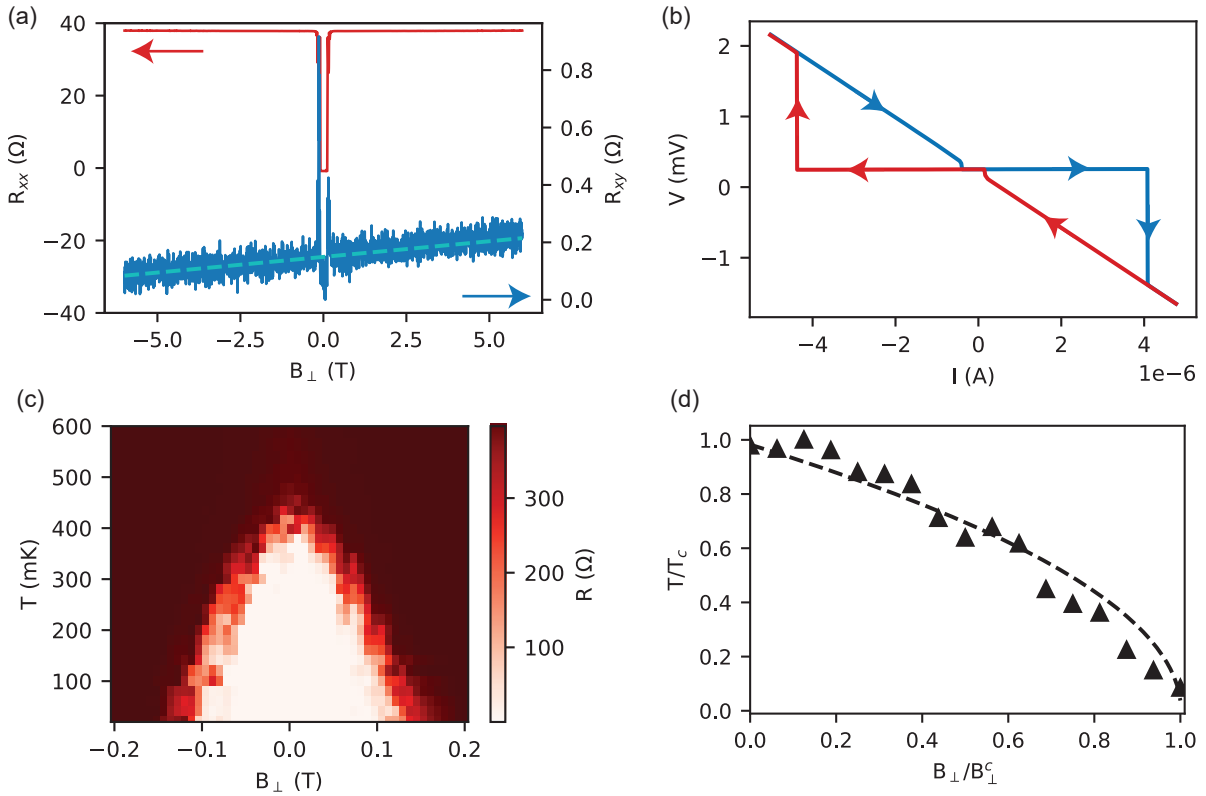


FIG. S6. **(a)** Longitudinal (red) and hall (blue) resistance of Hall bar HB3 for a symmetric out of plane magnetic field range of -6 T to 6 T. A linear fit of the Hall resistance of the device in the normal state is shown in the cyan dashed line, resulting in an estimated carrier density of $5.2 \times 10^{16} \text{ cm}^{-2}$. We estimate the mobility of the carriers in the PtSiGe Hall bar (aspect ratio $L/W = 2$) to be $6 \text{ cm}^2/\text{Vs}$. **(b)** Critical current measurements on a 100 nm wide PtSiGe wire at zero magnetic field and at base cryostat temperature. Arrows indicate the direction of the sweep. A critical current density of $2.7 \text{ A}/\text{m}^2$ is extracted assuming a PtSiGe thickness of 15 nm. **(c)** Critical out-of-plane magnetic field as a function of temperature recorded at the mixing chamber plate of the cryostat. Instabilities in PID loop impart approximately a $\pm 10 \text{ mK}$ error bar on the temperature axis. A critical temperature of $T_c = 408 \text{ mK}$ and critical out-of-plane magnetic field of 0.116 T are extracted from sigmoid function fits to the data. **(d)** Fitted critical temperature and magnetic field from c) scaled by their $B_{\perp}^c(T=0)$ and $T^c(B_{\perp}=0)$ values respectively. The dashed line is a BCS theory fit to the data.

Section V. Modeling of Subgap States

The device in the main text consists of a QD weakly coupled to one superconducting lead, and strongly coupled to another. We therefore write the Hamiltonian of the total system as:

$$H = H_{QD} + H_T + H_{SC}. \quad (1)$$

Where H_{QD} is defined as

$$H_{QD} = \sum_{\sigma} \epsilon d_{\sigma}^{\dagger} d_{\sigma} + U d_{\downarrow}^{\dagger} d_{\downarrow} d_{\uparrow}^{\dagger} d_{\uparrow} + \frac{E_z}{2} (d_{\uparrow}^{\dagger} d_{\uparrow} - d_{\downarrow}^{\dagger} d_{\downarrow}) \quad (2)$$

Here, ϵ is the electrochemical potential, U is the charging energy and E_z is the Zeeman energy. As one superconducting lead is weakly coupled, we consider only one bulk superconductor for H_{SC} , and ignore possible phase differences between their order parameters. In the superconducting Anderson impurity model, H_{SC} consists of a sum over multiple orbitals in the superconductor. Following Refs. [4, 5], we replace this sum by a single orbital and write:

$$H_{SC} = \xi \sum_{\sigma} c_{\sigma}^{\dagger} c_{\sigma} - \Delta (c_{\uparrow}^{\dagger} c_{\downarrow}^{\dagger} + h.c.) + \frac{E_z^{SC}}{2} (c_{\uparrow}^{\dagger} c_{\uparrow} - c_{\downarrow}^{\dagger} c_{\downarrow}) \quad (3)$$

Where ξ is the single-electron energy, Δ is the parent gap and E_z^{SC} is the Zeeman energy. We set $\xi = 0$, as the superconductor is grounded throughout the experiment. The Zeeman splitting of the superconductor is commonly excluded, as metallic superconductors usually have significantly lower g factors than the semiconductors they are coupled to. We however choose not to exclude it, in view of the low in-plane g-factor of Ge/SiGe heterostructure QDs, as well as the little-known magnetic field behavior of the novel PtGeSi superconductor. Finally, we can write the coupling of the superconductor and QD as:

$$H_T = \Gamma_S \sum_{\sigma} (c_{\sigma}^{\dagger} d_{\sigma} + h.c.) \quad (4)$$

where Γ_S is the spin-conserving hybridization energy. The full basis consists of 16 states, which we write as the tensor product of the number states of the superconductor and QD $|SC, QD\rangle$:

$$\{|0, 0\rangle, |\uparrow, 0\rangle, |\downarrow, 0\rangle, |2, 0\rangle, |0, \uparrow\rangle, |\uparrow, \uparrow\rangle, |\downarrow, \uparrow\rangle, |2, \uparrow\rangle, |2, \downarrow\rangle, |\uparrow, \downarrow\rangle, |\downarrow, \downarrow\rangle, |2, \downarrow\rangle, |0, 2\rangle, |\uparrow, 2\rangle, |\downarrow, 2\rangle, |2, 2\rangle\} \quad (5)$$

To model the spectrum, we consider excitations between the even and odd parity states. As the tunnel probe is a superconductor, we offset all excitation energies by Δ .

In Main Text Fig. 4b,c a Zeeman splitting of the superconductor was required to match the model to the experiment. For the model overlays seen in main text Figure 4a-c, the parameters used were a superconducting gap of $\Delta = 71 \mu\text{eV}$, a charging energy of $U = 1.6 \text{ meV}$, a hybridization energy of $\Gamma_S = 110 \mu\text{eV}$ along with an energy splitting on both SC and QD. We phenomenologically include the magnetic field dependence of the parent gap as: $\Delta(B) = 2\Delta_0 \sqrt{1 - (B/B_c)^2}$, where the factor of 2 is due to both leads having a superconducting density of states, resulting in quasiparticle transport between the bulk superconductors at $E = 2\Delta$ and $B_c = 0.9 \text{ T}$ as the critical field. This is required for agreement between the experimental data and the model, as states are observed at $E_{\text{state}} + \Delta$ due to the superconducting tunnel probe.

Using the described ZBW model we can compute the energy spectrum of the QD hybridizing with the SC. In S7d and g, we adding a Zeeman energy of $E_z = 56 \mu\text{eV}$ to the QD energy and nothing on the superconductor, which results in a spin-splitting at the charge degeneracy points $\epsilon(\Delta) = 0$ and $\epsilon(\Delta) = -1.6$, but no splitting in the even parity regions ($|S\rangle$), contradicting the data in Figure S7g. In supplement Figure S7e and h, we add a Zeeman energy of $E_z=56 \mu\text{eV}$ only to the SC, resulting in a splitting in the even parity states ($|S\rangle$) resembling the energy separation seen in main text Figure 4b-c, however we see no spin-splitting at the charge degeneracy points $\epsilon(\Delta) = 0$ and $\epsilon(\Delta) = -1.6$; furthermore, the characteristic eye-like curvature of the $|D\rangle$ state is significantly reduced, and does not match the data in Figure S7h. In Figure S7f and i, a Zeeman energy $E_z=56 \mu\text{eV}$ was added to both the QD and the SC, resulting in qualitative agreement to the data in Figure S7i. We stress that our model is quite simple and is not meant to fit the data quantitatively, and as such the magnitude and sign of the respective Zeeman terms have not been varied extensively. For example, future theoretical work could include the spin-orbit coupling, as well as a more detailed description of the superconductor beyond zero band width.

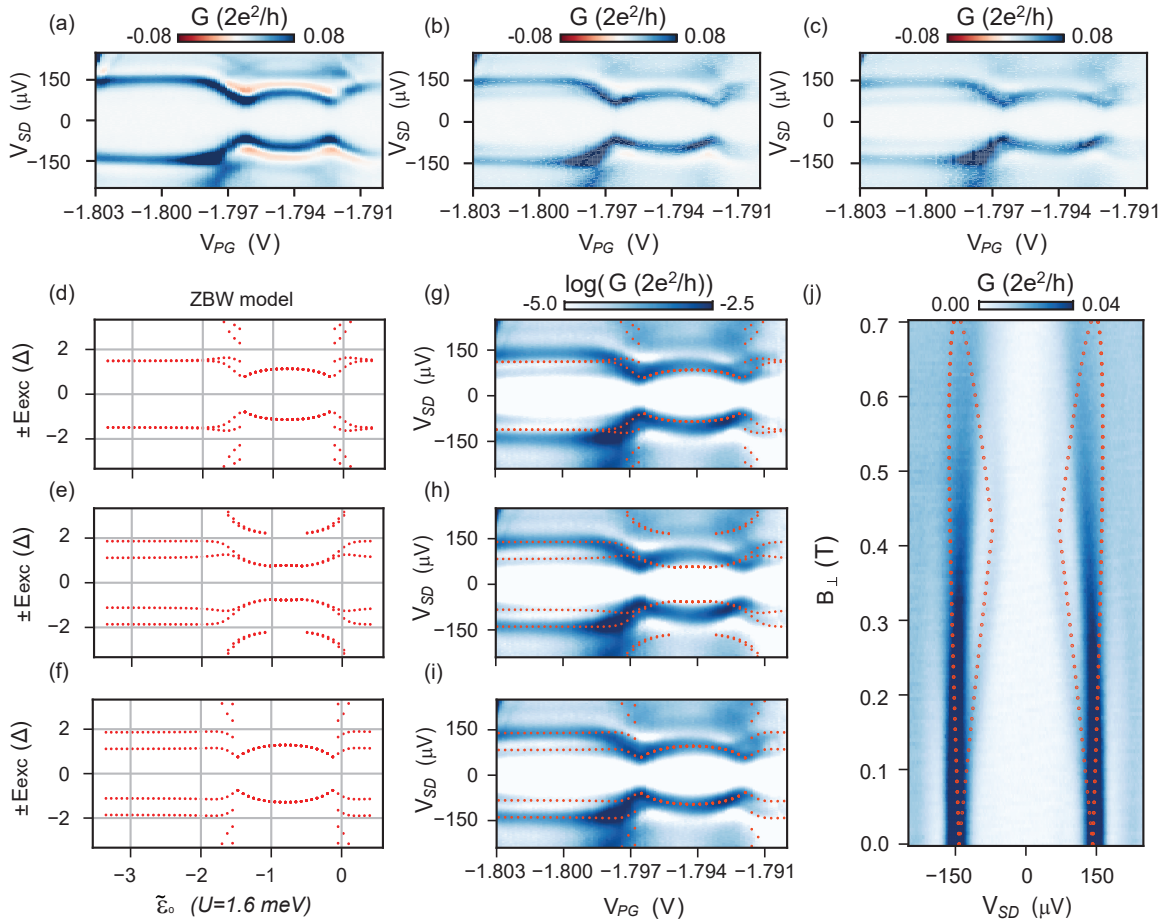


FIG. S7. **(a-c)** Bias spectroscopy data from main text Figures 4(a-c) without the logarithmic scale. **(d)** Excitation energy in units of $\Delta = 71\mu\text{eV}$ as a function of chemical potential in units of charging energy $U = 1.6\text{ meV}$, with a Zeeman energy only on the QD of $E_z=56\mu\text{eV}$. **(e)** Excitation energy in units of $\Delta = 71\mu\text{eV}$ as a function of chemical potential in units of charging energy $U = 1.6\text{ meV}$, with a Zeeman energy of $E_z=56\mu\text{eV}$ on SC only. **(f)** Excitation energy in units of $\Delta = 71\mu\text{eV}$ as a function of chemical potential in units of charging energy $U = 1.6\text{ meV}$, Zeeman energy on both SC and QD of $E_z=56\mu\text{eV}$. **(g-i)** Bias spectroscopy data from main Figure 4c, overlaid with the computed model (red) from supplement Figure 4d-f respectively. **(j)** Bias spectroscopy data from main Figure 4d overlaid with the computed ZBW model (orange) correcting for the gap closing as the magnetic field increases using a g-factor of 1.5 on both SC and QD.

Finally, in Fig S7j we show the bias spectroscopy data from main text Figure 4d, overlaid with the computed ZBW spectrum. There is a good agreement between the model and the data until about 400 mT, when the splitting becomes larger than the SC pairing energy. We attribute this discrepancy between model and data to the ZBW model, which cannot model the Zeeman effect on a bulk superconducting density of states.

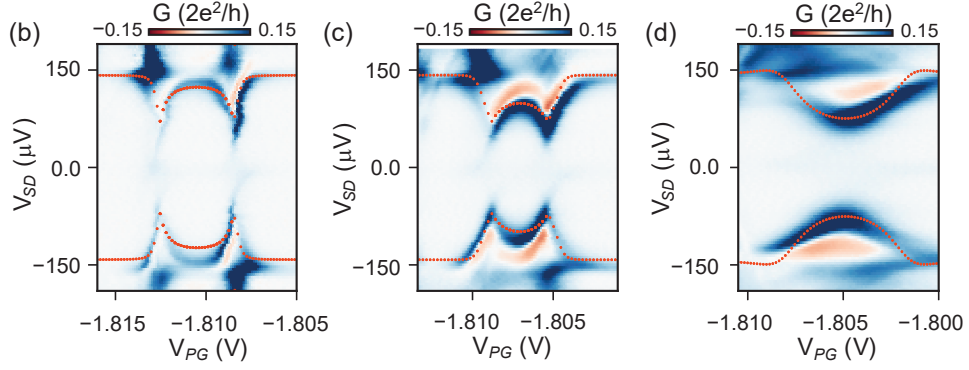


FIG. S8. (a) Bias spectroscopy data from main text Figure 2b overlaid with the computed ZBW model, setting the gap energy to $\Delta = 71 \mu\text{eV}$, a charging energy of $U = 1.6 \text{ meV}$ and a $\Gamma_S = 70 \mu\text{eV}$. (b) Bias spectroscopy data from main text Figure 2c overlaid with the computed ZBW model, setting the gap energy to $\Delta = 71 \mu\text{eV}$, a charging energy of $U = 1.6 \text{ meV}$ and a $\Gamma_S = 110 \mu\text{eV}$. (c) Bias spectroscopy data from main text Figure 2d overlaid with the computed ZBW model, setting the gap energy to $\Delta = 71 \mu\text{eV}$, a charging energy of $U = 1.6 \text{ meV}$ and a $\Gamma_S = 150 \mu\text{eV}$.

In order to quantify the hybridization energy of SC and QD Γ_S , we model the subgap states in main text Figure 2b-d in the ZBW model, using the superconducting gap and charging energy extracted in the main text. We manually tune the parameter Γ_S until a qualitative match between data and model is found. For Figures S8a-c we set the SC gap to $\Delta = 71 \mu\text{eV}$ and the charging energy to $U = 1.6 \text{ meV}$, for which we extract an estimate of $\Gamma_S = 70 \mu\text{eV}$ for Figures S8a, $\Gamma_S = 110 \mu\text{eV}$ for Figure S8b, and $\Gamma_S = 150 \mu\text{eV}$ for the fully coupled groundstate in Figure S8c.

[†] These authors contributed equally.

* anasua.chatterjee@tudelft.nl

- [1] F. Vigneau, F. Fedele, A. Chatterjee, D. Reilly, F. Kuemmeth, M. F. Gonzalez-Zalba, E. Laird, and N. Ares, Probing quantum devices with radio-frequency reflectometry, *Applied Physics Reviews* **10**, 021305 (2023).
- [2] A. Tosato, V. Levajac, J.-Y. Wang, C. J. Boor, F. Borsoi, M. Botifoll, C. N. Borja, S. Marti-Sanchez, J. Arbiol, A. Sammak, M. Veldhorst, and G. Scappucci, Hard superconducting gap in germanium, *Communications Materials* **4**, 23 (2023).
- [3] A. Ibabe, M. Gómez, G. O. Steffensen, T. Kanne, J. Nygård, A. L. Yeyati, and E. J. H. Lee, Joule spectroscopy of hybrid superconductor–semiconductor nanodevices, *Nature Communications* **14**, 2873 (2023).
- [4] T. Meng, S. Florens, and P. Simon, Self-consistent description of Andreev bound states in Josephson quantum dot devices, *Physical Review B* **79**, 224521 (2009).
- [5] J. Bauer, A. Oguri, and A. Hewson, Spectral properties of locally correlated electrons in a Bardeen–Cooper–Schrieffer superconductor, *Journal of Physics: Condensed Matter* **19**, 486211 (2007).